Advanced Energy Conversion Materials
http://ojs.wiserpub.com/index.php/AECM/

UNIVERSAL WISER PUBLISHER

Research Article

Study on Structural Stability of ZrO_2 and YSZ: Doping-Induced Phase Transitions and Fermi Level Shift

D. D. Nematov[1*], A. S. Burkhonzoda[1], Kh T. Kholmurodov[2,3], A. I. Lyubchyk[4], S. I. Lyubchyk[4], S. B. Lyubchyk[4]

[1]S.U.Umarov Physical-Technical Institute of the National Academy of Sciences of Tajikistan, 734042 Dushanbe, Tajikistan
[2]Joint Institute for Nuclear Research, Dubna, 141980 Moscow Region, Russia
[3]Dubna State University, Dubna, 141980 Moscow Region, Russia
[4]University Lusofona, 1749-024 Lisboa, Portugal
E-mail: dilnem@mail.ru

Received: 20 September 2023; **Revised:** 13 November 2023; **Accepted:** 14 November 2023

Abstract: This work summarizes the results of structural stability, electronic properties and phonon dispersion studies of biocompatible ZrO_2 compound in its cubic (c-ZrO_2), tetragonal (t-ZrO_2) and monoclinic (m-ZrO_2) phases. The authors found that the monoclinic phase of zirconium dioxide is the most stable among the three phases in terms of total energy, lowest enthalpy, highest entropy, and other thermodynamic properties. The presence of rather weak frequencies for m-ZrO_2 also confirms the monoclinic phase as a stable conformation of zirconia. Our analysis of the electronic properties showed that during the m-t phase transformation of ZrO_2, the Fermi level first shifts by 0.125 eV toward higher energies and then decreases by 0.08 eV in the t-c cross-section. The band gaps for c-ZrO_2, t-ZrO_2, and m-ZrO_2 are 5.140 eV, 5.898 eV, and 5.288 eV, respectively. Calculations to study the effect of 3.23, 6.67, 10.35 and 16.15 mol%Y_2O_3 on the structure and properties of m-ZrO_2 showed that the enthalpy of m-YSZ decreases linearly and accompanies further stabilization of zirconium dioxide. Doping-induced phase transitions of ZrO_2 were discovered under the influence of Y_2O_3 doping, due to which the position of the Fermi level changes and the band gap decreases. It has been established that, not only for pure systems but including those doped with Y_2O_3, the main contribution to the formation of the conduction band is made by the p-states of electrons.

***Keywords*:** zirconium dioxide, stability, oxygen vacancy, doped-induced phase transition, fermi level shift

1. Introduction

With the continuing threat of energy crisis and global warming caused by the increasing use of fossil fuels, the search for environmentally friendly energy sources is one of the most urgent tasks in the 21st century [1-2]. The development of green energy is one of the ways to mitigate the growing threat of global environmental problems and energy crisis, which is intensively growing worldwide. Solar panels and wind turbines have already become commonplace for mankind. However, new advances in nanotechnology and material science make it possible to obtain energy from other sources and will help to realize Nikola Tesla's creative idea of "To get electric current from air". Recently, scientists and engineers have been working on the development of innovative devices for converting moisture

DOI: https://doi.org/10.37256/aecm.5120243686

into electricity, which will expand the range of known renewable energy sources due to a new source of atmospheric moisture (galvanic converters that convert air moisture into electricity). That is, such devices are capable of harvesting electricity from atmospheric moisture and producing electric current, similar to the way solar cells capture sunlight and generate electricity.

Zirconium ceramics have been extensively studied in recent years because of their excellent electrical, optical and mechanical properties. They are also biocompatible and have a wide range of biomedical applications. Tetragonal phase yttria-stabilized zirconia (Y-TZP) has been used in various medical applications since the 1980s, particularly for dental crowns [2]. In addition, bulk materials and nanocomposites based on ZrO_2 are used in electrochemical cells because of their high oxide ion conductivity and catalytic activity, low thermal conductivity and mechanical/chemical stability, as well as compatibility with electrolytes [3-4].

One of the advantages of zirconium dioxide ceramics is the presence of three crystalline forms with different properties [5-9]. There are the most stable monoclinic (baddeleyite mineral; m-ZrO_2), metastable tetragonal (medium temperature), and unstable cubic structure of zirconium dioxide (high temperature). High pressure-induced zirconia phases in the form of brucite (orthorhombic-I) and cotunnite (orthorhombic-II) are also known [10-11]. Pure zirconium dioxide undergoes a phase transformation from monoclinic to tetragonal (about 1173 °C) and then to cubic (about 2370 °C), accompanied by a change in volume and, consequently, strength [12-14]. For the application of zirconium dioxide in modern ion-conducting ceramic devices, it is important that the stabilized material has a sufficient level of conductivity and the necessary mechanochemical stability in both oxidizing and reducing atmospheres. Obtaining a stable material from zirconium dioxide is difficult due to the marked volume change during the phase transition. Stabilization of zirconium dioxide is achieved by replacing part of the Zr^{4+} ions with larger ions in the crystal lattice [15-17]. For example, numerous studies have shown that doping with polyvalent oxides, including certain concentrations of yttrium oxide, stabilizes the high-temperature cubic and tetragonal phases of ZrO_2 at room temperature. This also leads to an increase in oxygen vacancy concentration and oxygen ionic conductivity, which allows the stabilized ZrO_2 to be used as an electrolyte in fuel cells [17]. The ionic conductivity of ZrO_2 strongly depends on the phase modification and the content of stabilizing additives in the system, which is also evidenced by the phase diagram given in [18]. At the same time, experimental study of pure ZrO_2 single crystals grown from the melt is difficult, phase transformations occur in them during cooling; therefore, their doped structures (e.g., yttrium-doped ZrO_2 structure, YSZ) are usually studied. However, the chemical composition of the yttria-stabilized zirconia (YSZ) surface is much more complex than that of pure ZrO_2. In another work, Kobayashi et al. [19] found that YSZ decomposes slowly at about 250°C by t-m transformation. This t-m transformation is accompanied by microcracking and loss of strength of the material in a humid atmosphere. This t-m transformation also occurs in the presence of water or humid environments in zirconia-based ceramic materials, which is called low-temperature degradation or aging of ZrO_2 crystals. Over the past few decades, a large amount of work has been done on this topic involving many hypotheses and discussions, and the most credible hypothesis on the topic of YSZ is based on the filling of oxygen vacancies that were present in the matrix to maintain a stable t-YSZ phase. Thus, filling these O vacancies with water radicals, either O_2 or OH, destabilizes the YSZ phase. However, the mechanism of YSZ stabilization itself is not fully understood and is still the subject of much debate. Therefore, modeling the properties of ZrO_2 and their stabilized structures including YSZ is necessary as a starting point for a proper understanding of their fundamental properties. On the other hand, aspects of the Fermi level shift after doping of yttrium oxide in ZrO_2, as well as the influence of doping on their stabilization are still insufficiently studied due to the difficulty of their detection in experiment.

2. Ab-initio simulation details

Ab initio calculations were carried out on the basis of the density functional theory [20]. All three modifications of ZrO_2 (Figure 1a-c) were first relaxed using the generalized gradient approximation (GGA) functionals [21] and strongly constrained and appropriately normed (SCAN) [22]. To obtain the most accurate value of the ground state energy, the total energy was calculated in terms of the GGA exchange-correlation potential, and SCAN was used to correctly estimate the lattice parameters. The calculations were carried out using the Vienna Ab-initio Simulation Package (VASP 6.4.2) [23]. By comparing the total energy in the unit cell, the stability of the three phases of ZrO_2 was evaluated, and then a supercell with a size of 2 × 2 × 2 was created to simulate the effect of 3.23, 6.67, 10.34, and 16.15 mol% Y_2O_3 on

the stability of ZrO_2 in order to investigate doped-induced phase transitions of zirconium dioxide and evaluate the effect of Y_2O_3 doping on the position of the Fermi level, as well as the stability of this ZrO_2.

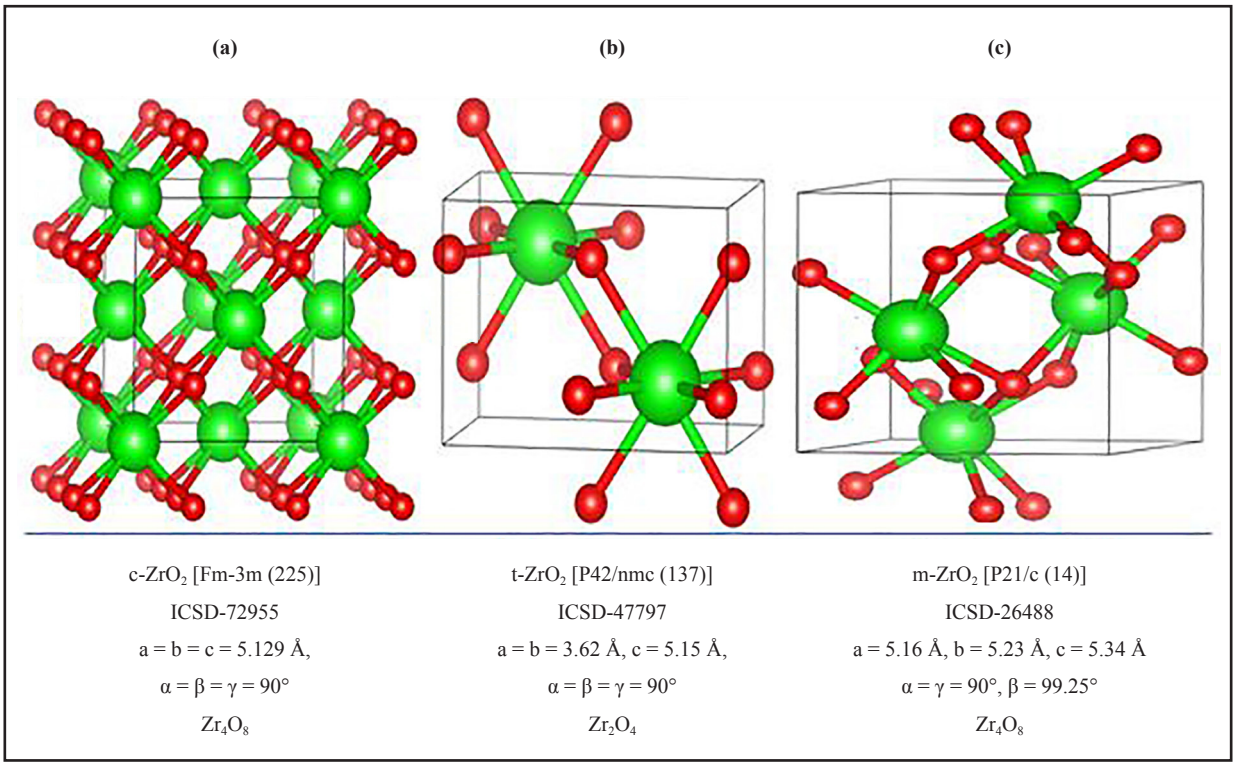

Figure 1. Crystal lattice models: a) cubic, b) tetragonal and c) monoclinic phase of ZrO_2

For yttrium oxide doping, some Y_2O_3 formula units were replaced by ZrO_2 in a 2 × 2 × 2 supercell, with one oxygen vacancy created in each substitution. A schematic description of the generation of YSZ-structures is made according to the scheme:

$$xZrO_2 + kY_2O_3 \rightarrow Zr_xY_{2k}O_{2x+3k} + V_{o_k}$$

$$\%Y_2O_3 = \frac{k}{x+k} \times 100\% \quad (1)$$

This can be thought of as combining x ZrO_2 formula units with k Y_2O_3 formula units arranged in an initial lattice of $x + k$ ZrO_2 units, resulting in the formation of m oxygen defects. Based on this, the authors determine the percentage of vacancy equal to the percentage of yttrium units in the final structure. Thus, our calculations were implemented for 4 different concentrations of Y_2O_3 doping (Table 1), which were refined using formula 1.

Vacancies were taken into account by removing one O atom with each subsequent substitution of 2 Y^{3+} ions in the Zr^{4+} position. The atomic orbitals O (2s, 2p), Zr (4d, 5s) and Y (4s 4p 4d 5s) were considered as valence electrons, while the remaining electrons were considered as nucleus electrons and remained frozen. The Projector augmented wave (PAW) method has been used to describe the interaction between valence electrons and electrons in the nucleus. The cutoff of the kinetic energy was fixed at the level of 600 eV, and all calculations were carried out taking into account spin-polarized effects. Orbital analyzes were performed by summing the contributions of individual atomic varieties in the

unit cell and showing the contributions of the main atoms at the meeting point of the valence band and the conduction band.

Table 1. Number of Zr, Y, O ions and oxygen vacancy for various mol. % Y_2O_3

mol. %Y_2O_3	Zr	Y	O	O vacancy	System
0	32	0	64	0	Zr32O64
3.23	30	2	63	1	Zr30Y2O63
6.67	28	4	62	2	Zr28Y4O62
10.35	26	6	61	3	Zr26Y6O61
16.15	22	10	59	5	Zr22Y10O59

3. Results and discussion

3.1 *Structural, electronic and phonon properties of ZrO_2*

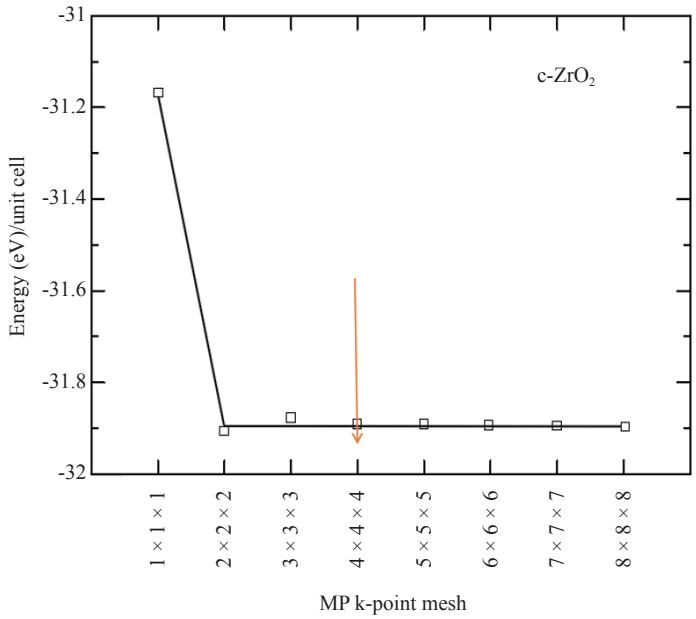

Figure 2. Total energy of the c-ZrO_2 unit cell as a function of the number of k-points (in the ENCUT = 1.3*ENMAX condition)

At the first step of the study, the geometry of pure ZrO_2 phases was optimized using the VASP package. To find the optimal value of the cutoff energy (ENCUT) and the appropriate number of k-points in the Brillouin zone, the authors tested the convergence of the total unit cell energy as a function of ENCUT and KPOINTS. The results of the convergence test for the number of k-points for the ZrO_2 cubic phase are shown in Figure 2, performed to build a k-point grid with a starting value of ENCUT = 1.3*ENMAX. Based on the results, it can be concluded that a 4x4x4 k-point grid with the Monkhrost-Pack scheme is optimally suited for the geometric relaxation of ZrO_2. However, when calculating

the electronic structure of these compounds, the number of k-points was at least doubled in order to obtain the most accurate density of states (DOS).

Similar tests were carried out to establish the cutoff energy, from which it can be seen that the choice of ENCUT = 600 eV is suitable for modeling ZrO_2, and a further increase in this energy only increases the calculation time without affecting its accuracy (Figure 3). Therefore, all further calculations were carried out at 600 eV. Similar convergence tests have also been carried out for the tetragonal and monoclinic phases of ZrO_2 using the GGA potential, which are also consistent with the results for the cubic phase.

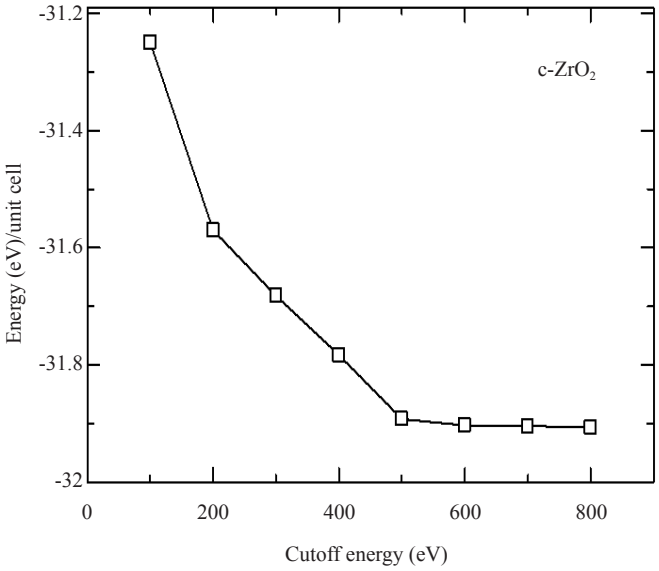

Figure 3. Total energy of the c-ZrO_2 unit cell versus cutoff energy (4 × 4 × 4 k-points)

Table 2 compares the calculated values of the lattice parameters of the ZrO_2 phase with the results from the literature.

According to the results given in Table 2, it can be seen that as the transition from a high-temperature phase to a lower-temperature phase, lattice distortion leads to a displacement of O ions in the c direction by a value of dz, expressed in relative units. As a result of distortion in the tetragonal phase, all Zr-O bonds will become nonequivalent. According to Table 2, the SCAN functionality describes the geometry much better than the standard GGA-PBE. Since the SCAN exchange-correlation function describes the structural properties well, the authors decided to use this function further when describing the geometry of other systems. The X-ray diffraction patterns of the initial structures obtained by us after their final relaxing are compared with the data from the literature, from which it can be seen that the results obtained by us are in good agreement with the experimental data, except for an imperceptible difference in the position of the X-ray peaks depending on the Bregg angles for the tetragonal system (Figure 4).

Table 3 compares the total energy calculated by the GGA method for the monoclinic, tetragonal, and cubic ZrO_2 phases, from which it can be seen that m-ZrO_2 is the most stable phase in terms of energy values compared to other phases, that is, the monoclinic ZrO_2 phase with space group P21/c is the most stable at low temperatures.

Table 2. Relaxed parameters of the ZrO_2 phase (The calculated results are compared with experimental and previous theoretical results)

	Lattice constants	This work		Exp.
		GGA	SCAN	
m-ZrO_2 [P2_1/c]	a (Å)	5.191	5.115	5.0950 [24]
	b (Å)	5.245	5.239	5.2116 [24]
	c (Å)	5.202	5.304	5.3173 [24]
	β°	99.639	99.110	99.230 [24]
	V (Å^3)	144.410	139.400	140.88 [24]
t-ZrO_2 [P4_2/nmc]	a = b (Å)	3.593	3.622	3.64 [25]
	c (Å)	5.193	5.275	5.27 [25]
	c/a	1.445	1.456	1.45 [25]
	V (Å^3)	67.05	69.214	69.83 [25]
	dz	0.012	0.013	0.046 [25]
c-ZrO_2 [Fm-3m]	a = b = c (Å)	5.075	5.12	5.129 [26-27]
	V(Å^3)	130.709	134.06	134.9 [26-27]

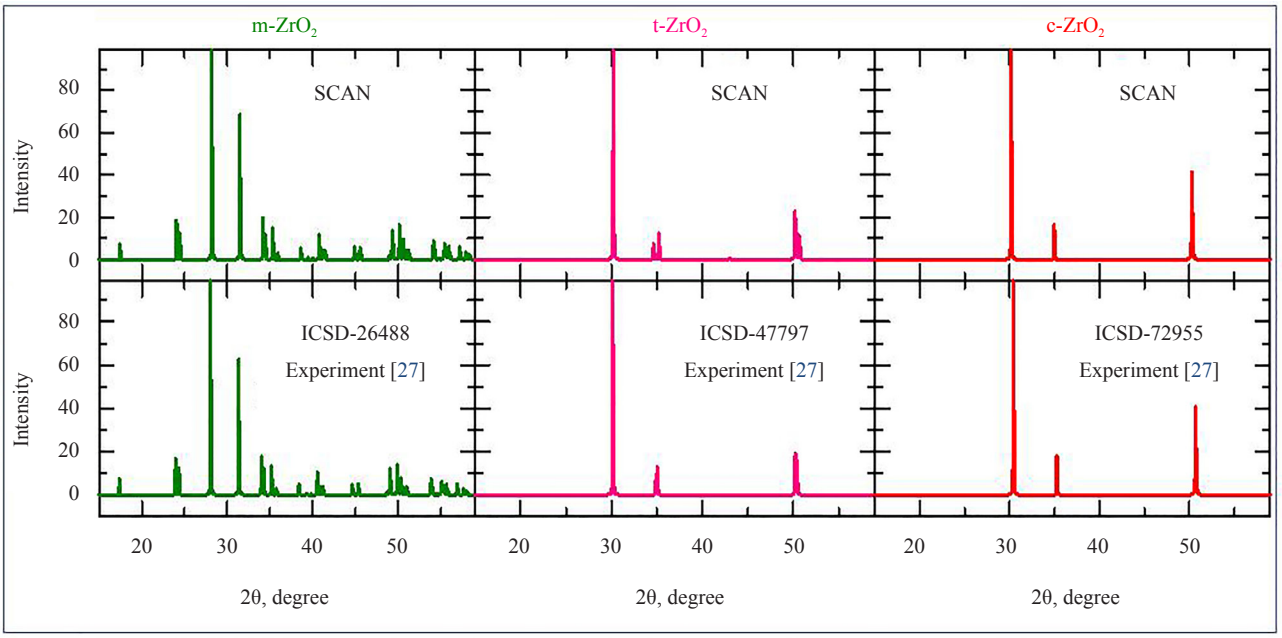

Figure 4. Comparison of experimental and calculated (SCAN) X-ray diffraction patterns of m-ZrO_2, t-ZrO_2, and c-ZrO_2

Table 3. GGA-calculated total electronic energies of c-ZrO_2, t-ZrO_2, m-ZrO_2 unit cells

System	Energy	ΔE
m-ZrO_2	-28.7947	0
t-ZrO_2	-28.6885	0.106
c-ZrO_2	-28.5865	0.201

Next, using the Phonopy code in the VASP package, the authors simulated the thermodynamic properties and phonon spectra of the ZrO_2 phase for a more detailed discussion of the structural stability of the ZrO_2 monoclinic phase. Figure 5 shows the change in the entropy of the unit cells of the ZrO_2 phase as a function of temperature.

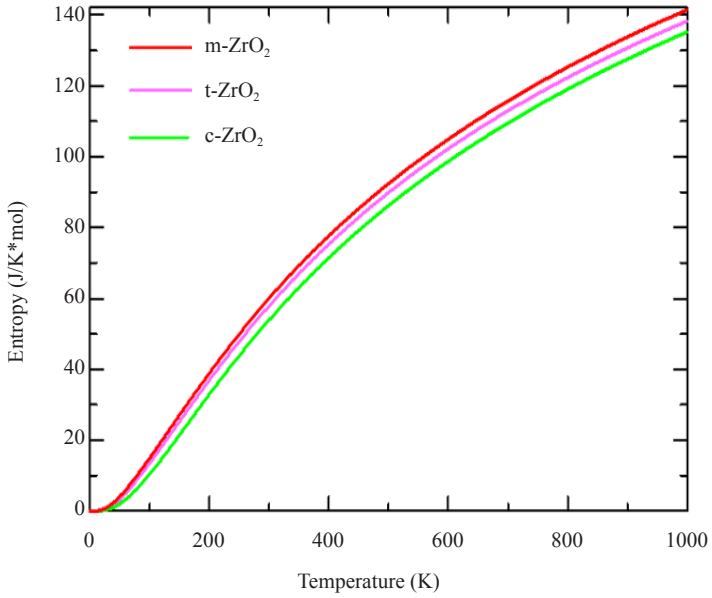

Figure 5. Entropy as a function of absolute temperature per unit cell c-ZrO_2, t-ZrO_2, m-ZrO_2

According to Figure 5, as the transition from the monoclinic to the tetragonal and cubic phases, the entropy of these compounds decreases, which corresponds to the criterion of inverse dependence of enthalpy or direct dependence of the entropy and stability of solid systems [28]. This pattern can also be clearly observed after analyzing the pattern of phonon frequencies of the three phases of ZrO_2 (Figure 6 a-c) from which it is clearly seen that the monoclinic phase has the smallest negative modes than the other two phases.

Figure 7a-c shows the temperature dependence of free energy, entropy and heat capacity for m-ZrO_2, t-ZrO_2 and m-ZrO_2.

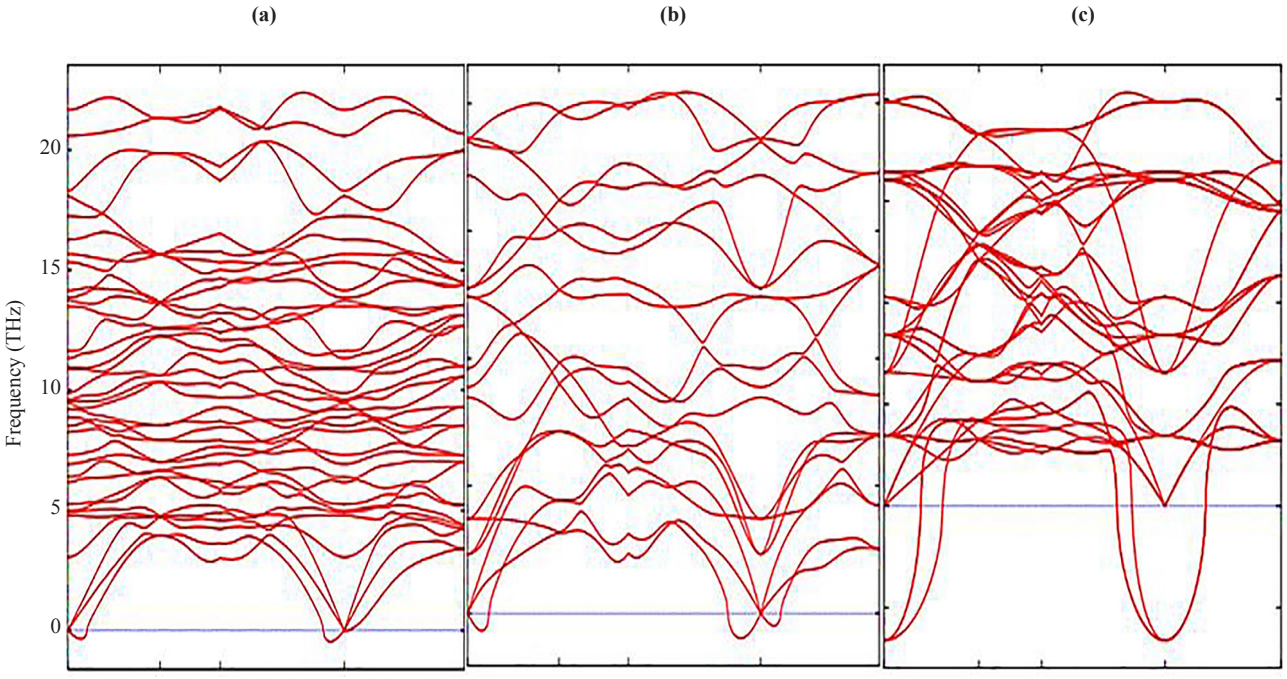

Figure 6. Phonon dispersion relations of (a) monoclinic, (b) tetragonal, and (c) cubic ZrO_2 at 0 K

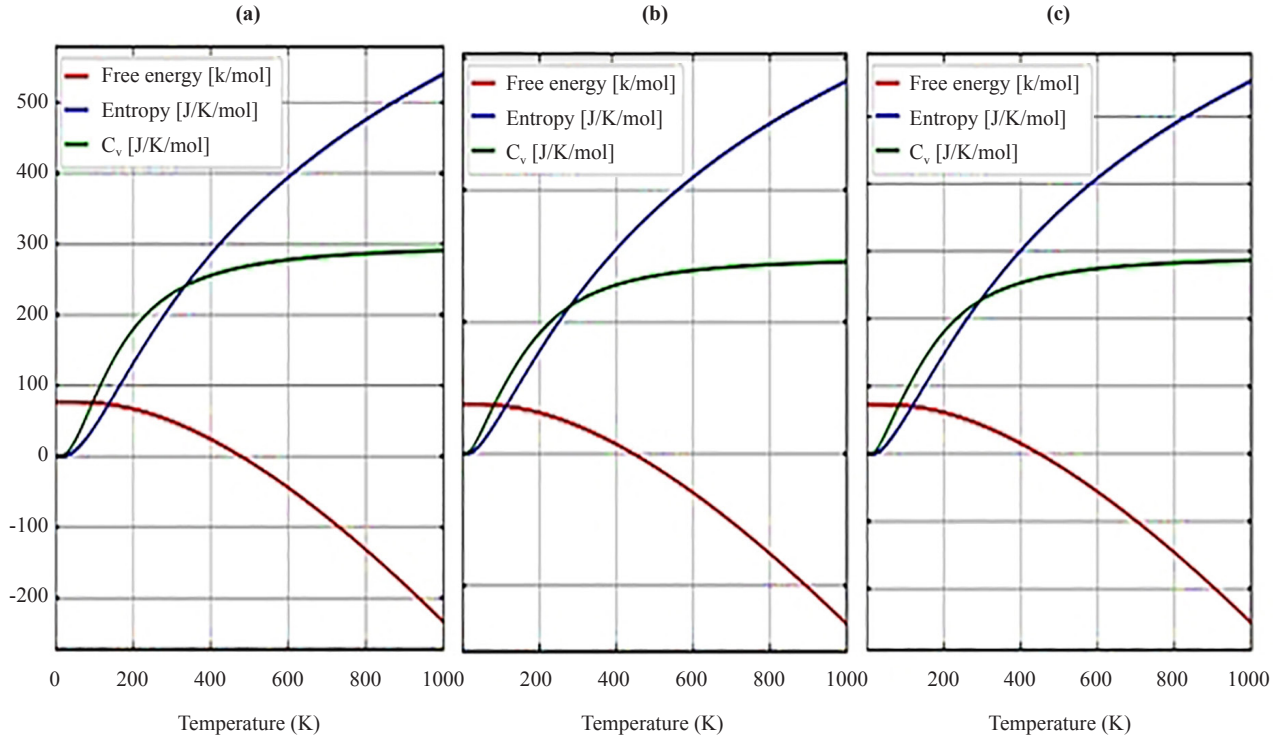

Figure 7. Temperature dependence of free energy, entropy and heat capacity for: m-ZrO_2 (a), t-ZrO_2 (b), and m-ZrO_2 (c)

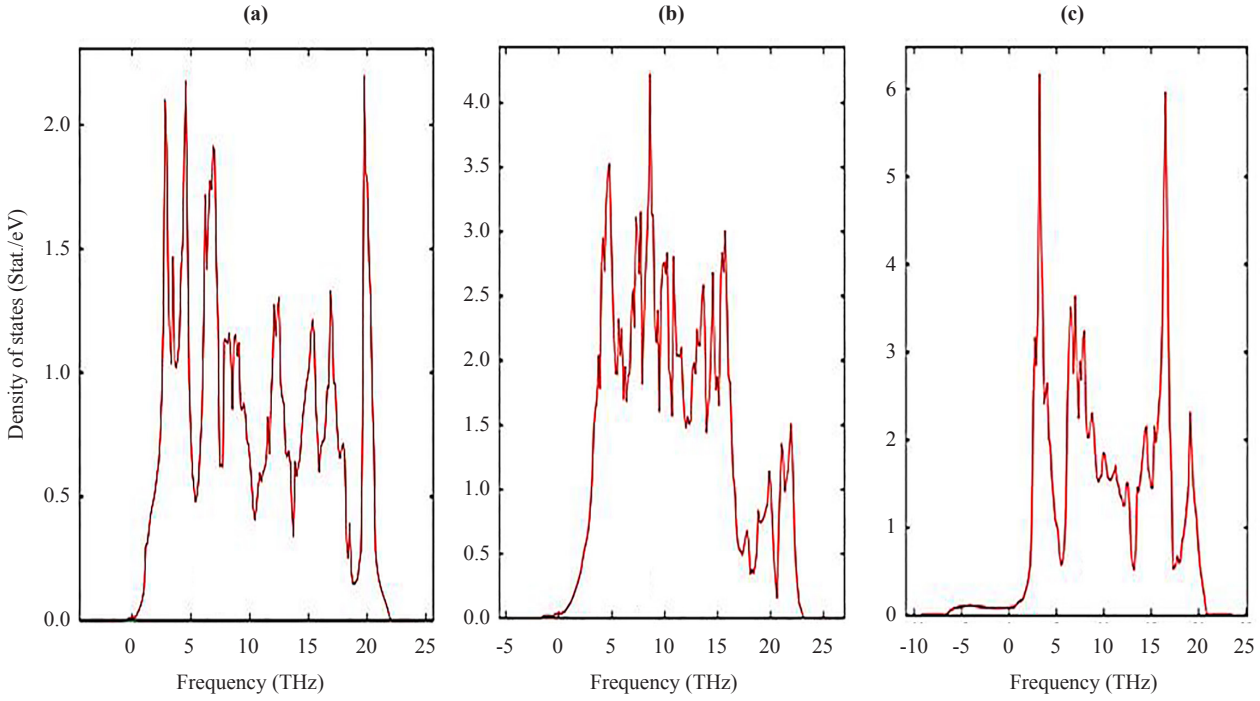

Figure 8. Phonon density of states for (a) m-ZrO_2, (b) t-ZrO_2, and (c) m-ZrO_2

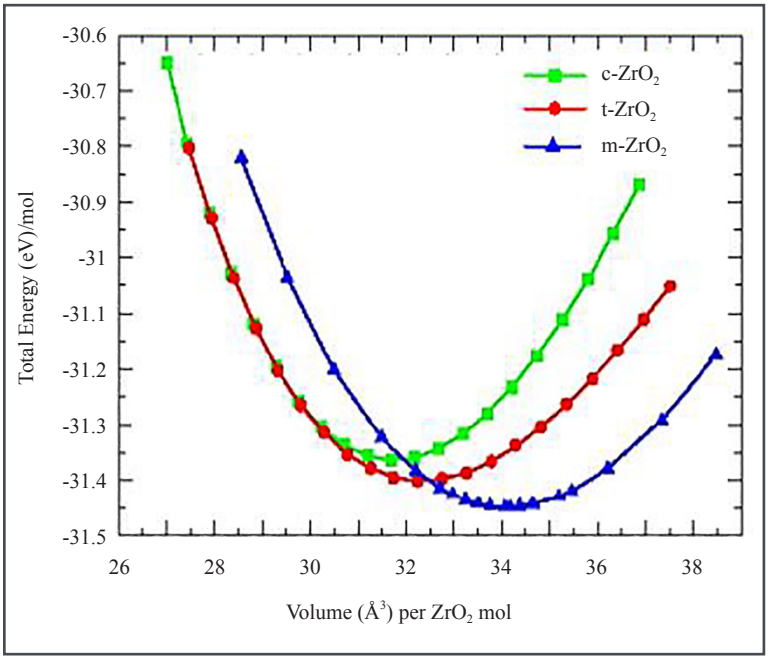

Figure 9. Total energy as a function of volume for m-ZrO_2 (a), t-ZrO_2 (b), and m-ZrO_2 (c)

The results of calculations of the density of phonon states are shown in Figure 8a-c indicating that as the transition from the monoclinic to the tetragonal and cubic phases, the density of electronic states increases, and they also correspond well with the results given in Figure 6 and confirm the monoclinic phase as the most stable among

other ZrO_2 phases. This is also confirmed by the result of the Energy/Volume diagram shown in Figure 9 and is in good agreement with literature data [29]. Therefore, for further stabilization by doping with Y_2O_3, the choice of the monoclinic phase is appropriate.

Table 4. Calculated and experimental band gap of c-ZrO_2, t-ZrO_2, m-ZrO_2 in eV

System	This work			Experiment [30]
	GGA	SCAN	HSE06	
m-Z_rO2	3.9	3.8	5.288	5.78
t-ZrO_2	4.42	4.37	5.898	5.83
c-ZrO_2	4.03	3.93	5.140	6.10

Next, using the well-optimized structures of the three phases of ZrO_2, the authors studied the electronic properties of these systems. Using the GGA, SCAN functionals and the HSE06 hybrid functional, the band gap values of these systems were found (Table 4), their orbital structure was analyzed, and the change in the position of the Fermi level in these systems was modeled.

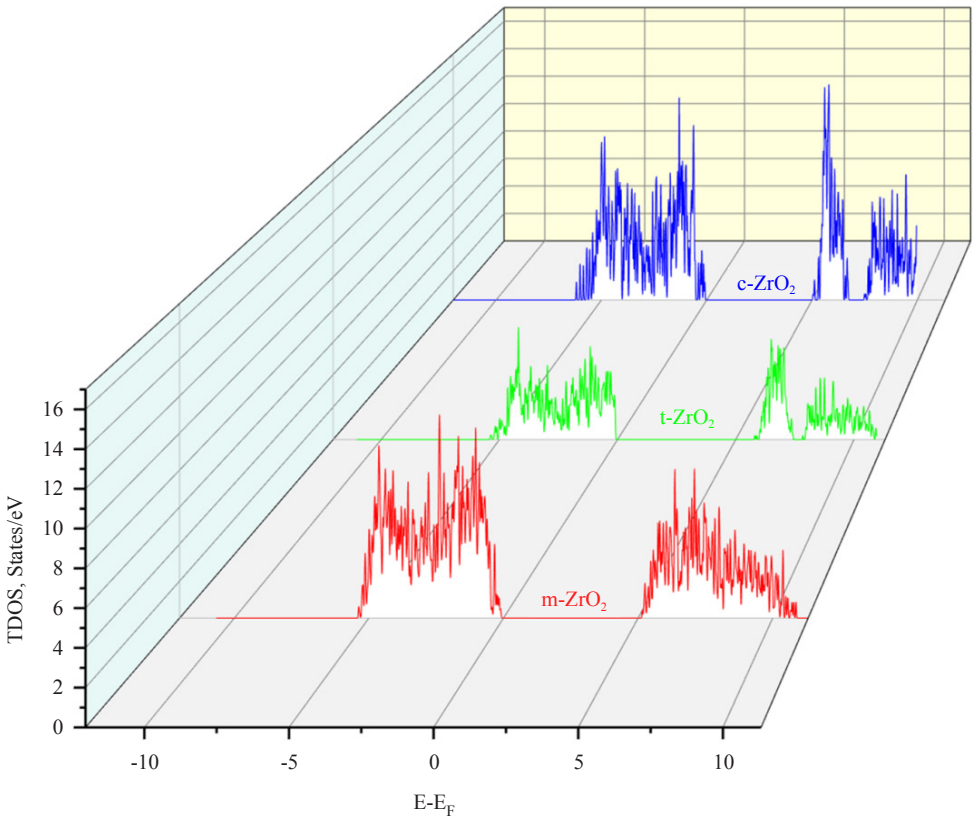

Figure 10. Total density of electron states (TDOS) of monoclinic, tetragonal, and cubic ZrO_2

According to the results presented in Table 3, the GGA and SCAN functionals showed a rather small band gap compared to the HSE06 hybrid functional [31], which traditionally overcomes underestimation of the band gap well. Given the suitability of HSE06 for estimating the band gap energy, the authors further used this particular hybrid functional to describe all problems related to the electronic properties of the systems under study.

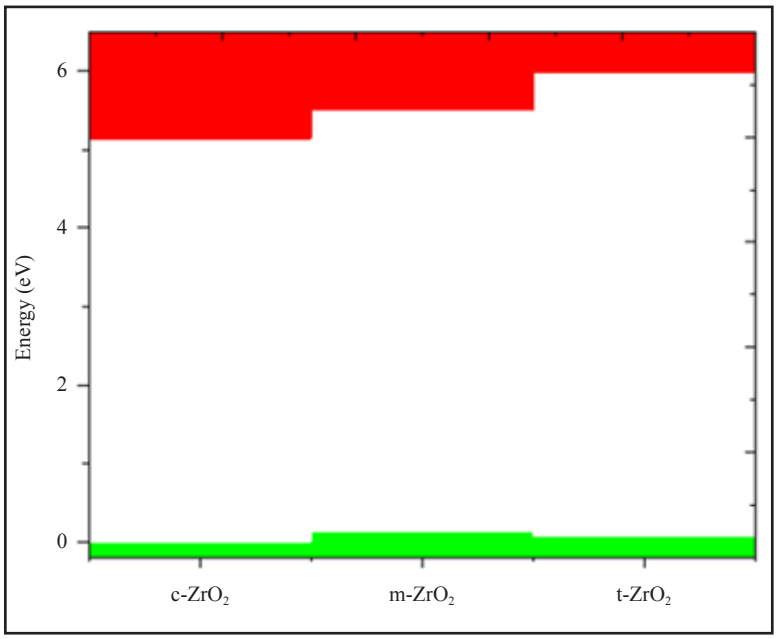

Figure 11. Conduction (red)-and valence (green)-band change for c-ZrO_2, t-ZrO_2, m-ZrO_2. Position of the Fermi level corresponds to the maximum of the valence band at each of the sites

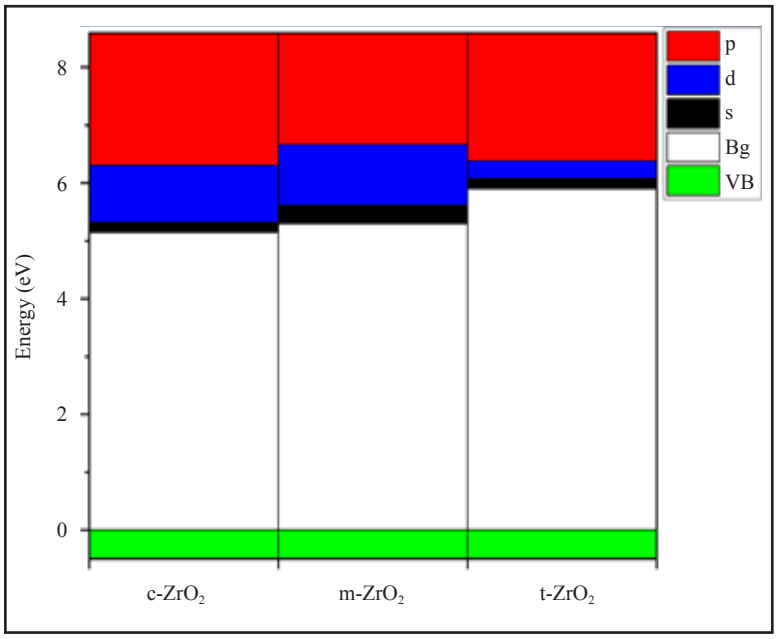

Figure 12. Composite PDOS diagram showing the main contributions of s-, p- and d-orbitals to the states that form the CB bottom for c-ZrO_2, t-ZrO_2, m-ZrO_2. Top of VB (green), scaled to zero

Next, using the ZrO_2 structures relaxed using the SCAN functional, calculations were made of the density of available electronic states at the Fermi level (Figure 10), which is crucial for interpreting the electronic properties of ZrO_2 and the transport characteristics of electronic devices based on it.

According to Figure 10, the density of electronic states for c-ZrO_2 is slightly overestimated compared to other phases. Moreover, secondary energy gaps are observed in the energy diagram of the tetragonal and cubic phases. Also, this gap increases with the transition from the tetragonal to the cubic phase.

Next, the authors determined the position of the Fermi level in ZrO_2 crystals and the shift of this level during their phase transformation. As can be seen from Figure 11, if the position of the Fermi level (maximum of the valence band) for the monoclinic phase is taken as the reference point, then during the m-t phase transformation of ZrO_2, this level first drops by 0.125 eV towards lower energies and then descends again in the t-c section by 0.08 eV. This is also observed in detail from the results of the summarized bands for the orbital analysis, which are shown in Figure 12 for the three phases of ZrO_2.

It can be seen from Figure 12 that as we move from the monoclinic to the tetragonal and cubic phase, the contribution of the p orbitals becomes more significant in CB, and the s orbitals make a small contribution, while the d state shows a different trend. It is assumed that this behavior may be associated with a change in the crystal field and covalence of ZrO_2 during the phase transformation.

3.2 *Stabilization of m-ZrO_2 and electronic properties of YSZ*

After the final preparation of YSZ-structures (according to the scheme proposed in formula 1 and Table 1), geometric optimization was carried out and Y_2O_3-doped ZrO_2 supercells were relaxed using the GGA and SCAN functionals. Table 5 shows the geometric parameters of the ZrO_2 and YSZ supercells at various Y_2O_3 concentrations after relaxation using the SCAN functional.

Table 5. Lattice parameters of 2x2x2 supercells of ZrO_2 and YSZ at various Y_2O_3 concentrations

System	Lattice parameters						Phase
	a (Å)	b (Å)	c (Å)	α (°)	β (°)	γ (°)	
0	10.23	10.478	10.608	90	99.64	90.00	m-YSZ
3.23 mol. %Y_2O_3	10.274	10.524	10.536	90.21	98.84	89.94	m-YSZ
6.67 mol. %Y_2O_3	10.512	10.544	10.603	89.90	90.12	89.62	t-YSZ
10.35 mol. %Y_2O_3	10.529	10.541	10.546	89.98	90.09	90.08	t-YSZ
16.15 mol. %Y_2O_3	10.540	10.541	10.543	90.08	90.00	90.02	c-YSZ

According to the results shown in Table 5, it can be seen that the doping of yttrium oxide, namely the concentration of more than 14 mol. %Y_2O_3 stabilizes the monoclinic phase of zirconia to a cubic phase. However, in this case, the lattice parameters of Y_2O_3-doped structures change non-linearly. Figure 13 shows the volume vibration of ZrO_2 lattices as a function of Y_2O_3 concentration (x).

According to Figure 14, with increasing doping concentration, the energy difference between the monoclinic phase with the tetragonal and cubic decreases, which indicates the possibility of doping-induced phase transitions of zirconium dioxide in the indicated Y_2O_3 doping concentration ranges.

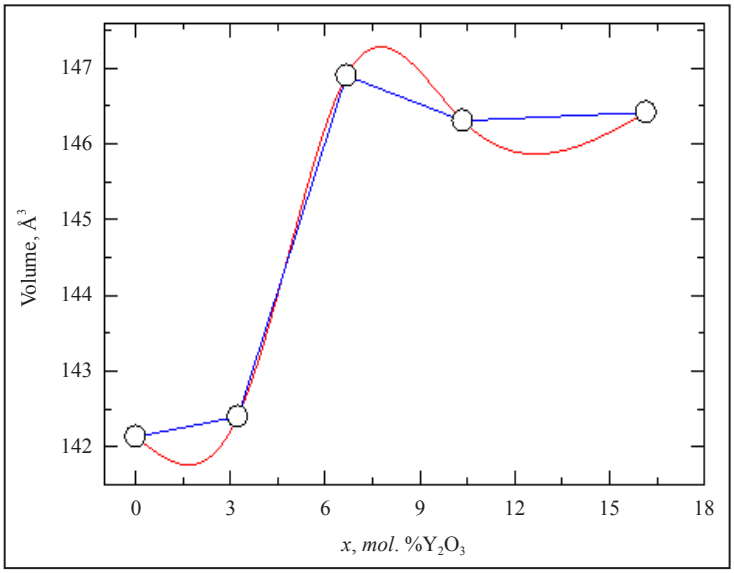

Figure 13. Vibrations of ZrO_2 volume as a function of Y_2O_3 concentration

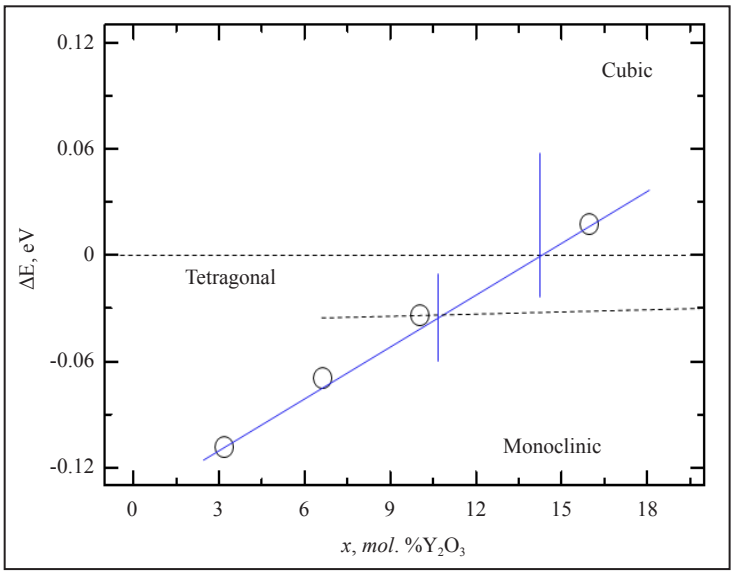

Figure 14. Total energy difference between unit cell phases of ZrO_2 as a function of Y_2O_3 doping concentration

Having obtained the optimized structures, the authors calculated the energy of formation (E_f) and enthalpy energy of formation (ΔH) for ZrO_2 and YSZ, as well as the energy of formation of a vacancy (E_{df}) for YSZ using the following formulas:

$$E_f = E_{tot} - \sum_x E_{tot}(x) \tag{2}$$

$$E_{df} = E_{tot}^{Zr_{32-x}Y_xO_{64-\delta}} - E_{tot}^{Zr_{32}O_{64}} + \delta \times E_{tot}^{O} \tag{3}$$

$$\Delta H = \frac{E_{YSZ} - \left[xE_{ZrO_2} + kE_{Y_2O_3} \right]}{x + k} \quad (4)$$

where E_{tot} is the total energy of the system, $E_{tot}(x)$ is the total energy of individual components, and δ is the number of vacancies (defects) in the crystal. The calculated values of E_f and E_{df} per atom are given in Table 6.

Table 6. GGA-calculated values of enthalpy (ΔH) and formation energy (E_f) for ZrO_2 and YSZ. Oxygen vacancy formation energy (E_{df}) for YSZ

System	ΔH	E_f	E_{df}
0	64.02917222	-4.747216667	0
3.23 mol. %Y_2O_3	59.91124404	-4.848422632	-1.874577368
6.67 mol. %Y_2O_3	56.13271879	-4.967857447	-3.739875532
10.35 mol. %Y_2O_3	52.7041267	-5.106527419	-5.596013441
16.15 mol. %Y_2O_3	47.00229139	-5.384704945	-9.220196154

Figure 15 shows a diagram of the dependence of the change in the enthalpy of the formation of YSZ on the concentration of Y_2O_3, calculated by formula 4, from which it is clearly seen that doping with Y_2O_3 reduces the enthalpy and leads to the stabilization of zirconium dioxide. The empirical formula obtained by the least squares method says that the enthalpy of formation energy decreases linearly according to the law ΔH = -1.0407x + 63.532, where x is the concentration of Y_2O_3 in YSZ.

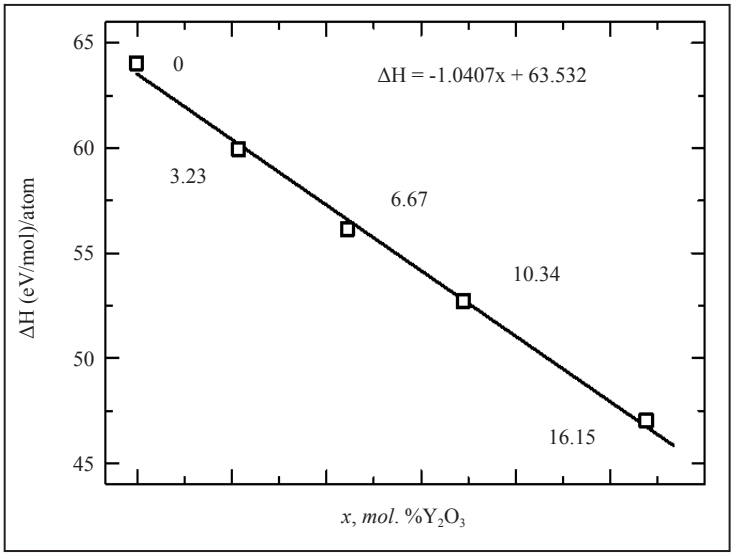

Figure 15. Enthalpy formation energy for YSZ as a function of Y_2O_3 concentration

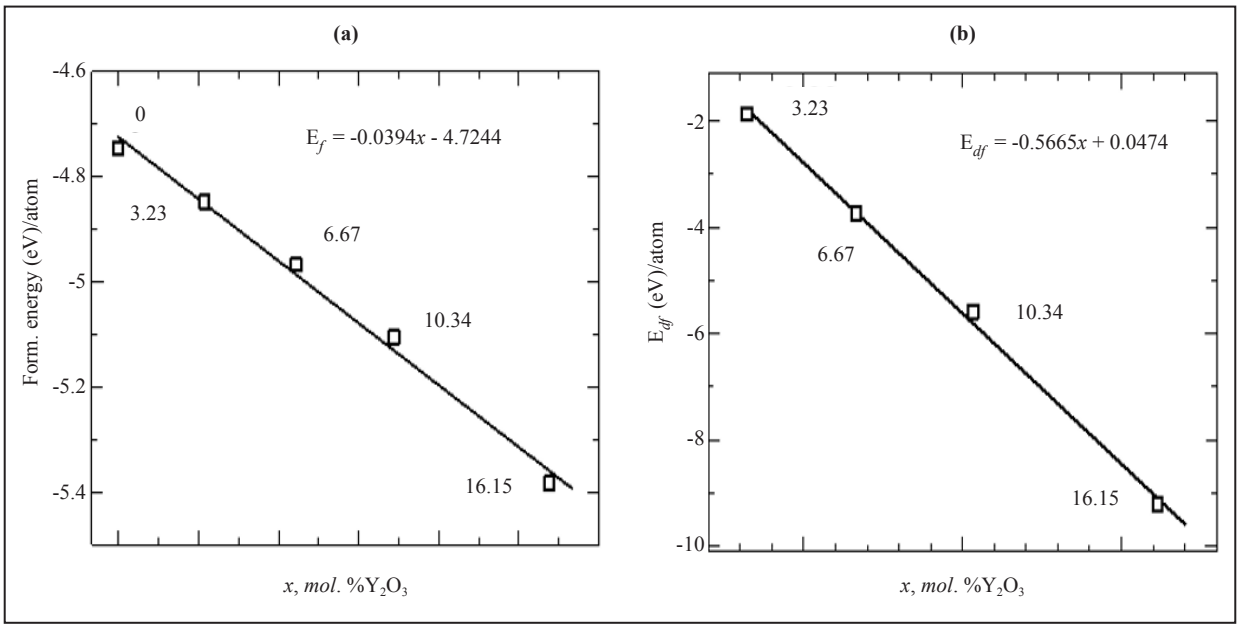

Figure 16. Energy of formation (a) and energy of formation of an oxygen vacancy (b) for YSZ as a function of Y_2O_3 concentration

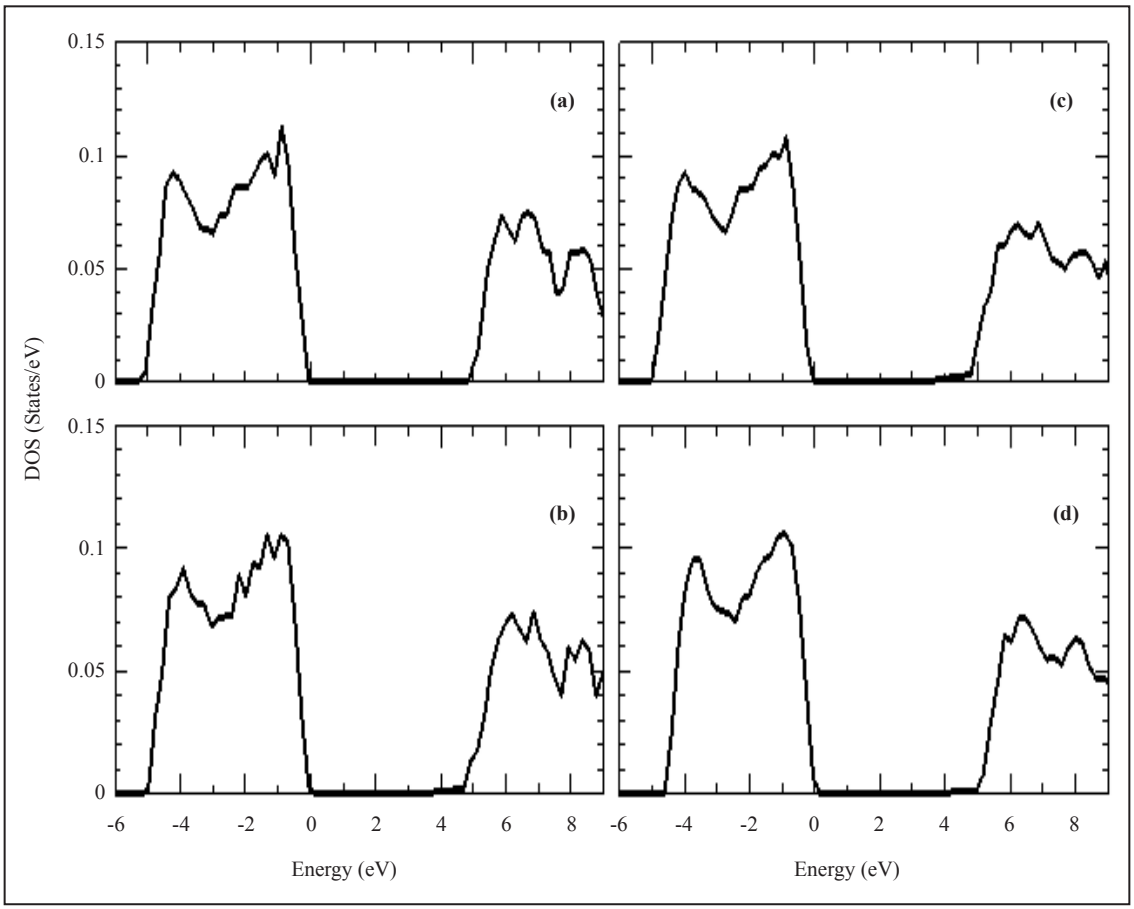

Figure 17. Total electron density of states (TDOS) for ZrO_2 doped with 3.23 (a), 6.67 (b), 10.34 (c), and 16.15 (d) mol% Y_2O_3

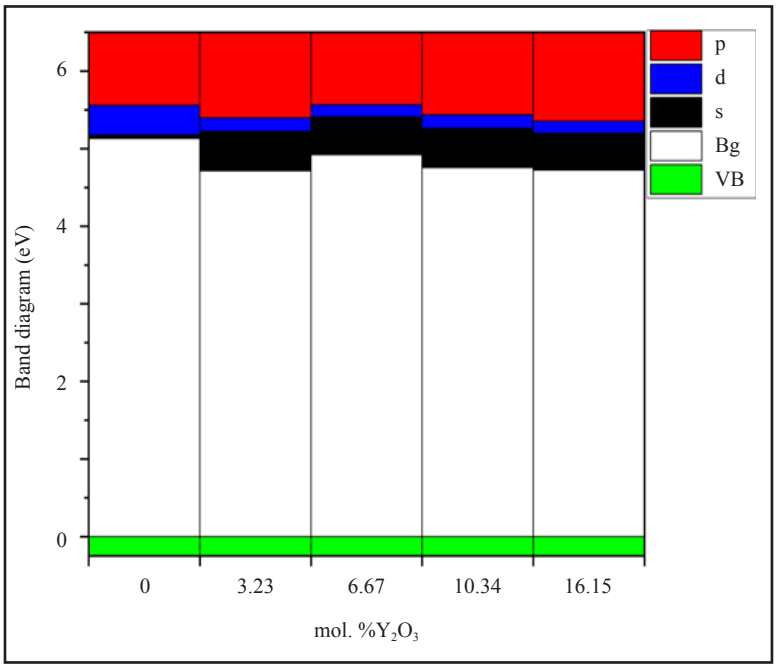

Figure 18. Composite PDOS diagram demonstrating the main contributions of s-, p- and d-orbitals to the states forming the CB bottom for ZrO_2 doped with 3.23, 6.67, 10.34 and 16.15 mol% Y_2O_3. Top of VB (green), scaled to zero

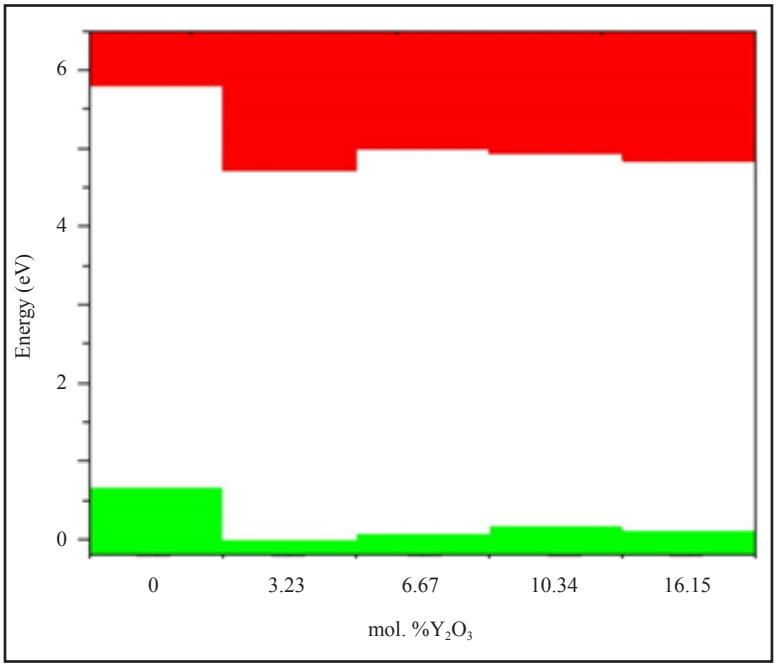

Figure 19. Conduction (red)-and valence (green)-band change for ZrO_2 doped with 3.23, 6.67, 10.34 and 16.15 mol% Y_2O_3. The position of the Fermi level corresponds to the maximum of the valence band at each of the sites

Thus, as the concentration of Y_2O_3 increases, the number of oxygen vacancies in YSZ increases, and the growth of these O vacancies is considered as a stabilizing mechanism for the monoclinic phase of zirconia, as evidenced by a decrease in the enthalpy of formation. The numerical value of the enthalpy formation energy is shown in Table 6.

Figure 16 shows the nature of the change in E_f and E_{df} from the concentration of yttrium oxide, from which the regularity of their linear decrease is clearly visible.

Next, calculations were carried out to study the electronic structure of Y_2O_3 stabilized ZrO_2 supercells to reveal in detail the effects of doping on their density of states, Fermi energy behavior, and orbital states. Figure 17 shows plots of the change in the density of electronic states YSZ for all doping concentrations of Y_2O_3.

According to the results presented in Figure 16, it can be seen that after Y_2O_3 doping in TDOS structures, no new energy states arise due to the introduction of defects, that is, it does not lead to a change, except for the band gap shift, which can be considered in detail after orbital analysis (Figure 18) and estimates of the shift of the Fermi level (Figure 18). The band gap is 4.71 eV, 4.92 eV, 4.75 eV, and 4.72 eV, respectively, for ZrO_2 with doped 3.23, 6.67, 10.34, and 16.15 mol% Y_2O_3.

According to Figure 19, after doping with 3.23 mol% Y_2O_3 in pure m-ZrO_2, the Fermi level drops by 0.067 eV and then shifts by 0.007 eV towards the conduction band when doped with 6.67 mol% Y_2O_3. Then, at a doping concentration of 10.34 mol%, it still rises by 0.01 eV, being 0.017 eV higher than in the case of 3.23 mol% Y_2O_3. However, after doping with 16.15 mol% Y_2O_3, it drops to 0.012 eV. According to the PDOS diagram, one can interpret and observe the step pattern of the conduction band with the contribution of s-, p- and d-orbitals. Understanding these features make it possible to tune the Fermi energies in the band structure for specific tasks in modern materials science and instrumentation. The results obtained will help to interpret some of the features of the electronic properties of ZrO_2 and solid materials [32-47], and also complement the base of scientific work carried out in the field of using biocompatible zirconium dioxide crystals and ceramics for generating green energy. The data can be used in the design of moisture-to-electricity converters and the creation of solid oxide fuels. cells based on ZrO_2.

4. Conclusion

In this work, using quantum-chemical calculations, phase transitions and stabilization of zirconium dioxide under the action of yttrium oxide doping, which has attracted great research interest in recent years, have been proved. By comparing the total energy and enthalpy it was proved that the monoclinic phase is most stable in a condition closer to ambient. It has been shown that the Fermi level changes during phase transitions and that doping of yttrium oxide increases the density of the state of zirconium dioxide. The calculations show that the presence of oxygen vacancies plays an important role in the phase transition and stabilization of ZrO_2. The obtained results enrich the data bank for a more detailed understanding of the mechanism of zirconium dioxide phase transitions, and can also be used to adjust the parameters of theoretical calculations for and description of other properties of zirconium dioxide, which are still beyond the limits of quantum-chemical modeling.

Funding

The research leading to these results has received funding from the European Union's Horizon 2020 research and innovation programme under the Marie Sklodowvska-Curie grant agreement 871284 project SSHARE.

Acknowledgment

The authors express their sincere gratitude to Dr. Mekhrdod S. Kurboniyon from Chongqing University of Posts and Telecommunications of the People's Republic of China for his valuable advice and guidance during the conduct of this study.

Conflict of interest

The authors declare no competing financial interest.

References

[1] Chu S, Cui Y, Liu N. The path towards sustainable energy. *Nature Materials*. 2017; 16(1): 16-22. Available from: https://doi.org/10.1038/nmat4834.

[2] Chu S, Majumdar A. Opportunities and challenges for a sustainable energy future. *Nature*. 2012; 488(7411): 294-303. Available from: https://doi.org/10.1038/nature11475.

[3] Shen D, Xiao M, Zou G, Liu L, Duley WW, Zhou YN. Self-powered wearable electronics based on moisture enabled electricity generation. *Advanced Materials*. 2018; 30(18): 1705925. Available from: https://doi.org/10.1002/adma.201705925.

[4] Shao C, Ji B, Xu T, Gao J, Gao X, Xiao Y, et al. Large-scale production of flexible, high-voltage hydroelectric films based on solid oxides. *ACS Applied Materials & Interfaces*. 2019; 11(34): 30927-30935. Available from: https://doi.org/10.1021/acsami.9b09582.

[5] Yashima M, Ohtake K, Arashi H, Kakihana M, Yoshimura M. Determination of cubic-tetragonal phase boundary in $Zr_{1-X}Y_XO_{2-X/2}$ solid solutions by Raman spectroscopy. *Journal of Applied Physics*. 1993; 74(12): 7603-7605. Available from: https://doi.org/10.1063/1.354989.

[6] Yashima M, Sasaki S, Kakihana M, Yamaguchi Y, Arashi H, Yoshimura M. Oxygen-induced structural change of the tetragonal phase around the tetragonal-cubic phase boundary in $ZrO_{2-Y}O_{1.5}$ solid solutions. *Acta Crystallographica Section B: Structural Science*. 1994; 50(6): 663-672. Available from: https://doi.org/10.1107/S0108768194006257.

[7] Yashima M, Kakihana M, Yoshimura M. Metastable-stable phase diagrams in the zirconia-containing systems utilized in solid-oxide fuel cell application. *Solid State Ionics*. 1996; 86: 1131-1149. Available from: https://doi.org/10.1016/0167-2738(96)00386-4.

[8] Yashima M, Ohtake K, Kakihana M, Arashi H, Yoshimura M. Determination of tetragonal-cubic phase boundary of $Zr_{1-X}R_XO_{2-X2}$ (R = Nd, Sm, Y, Er and Yb) by Raman scattering. *Journal of Physics and Chemistry of Solids*. 1996; 57(1): 17-24. Available from: https://doi.org/10.1016/0022-3697(95)00085-2.

[9] Yashima M, Ishizawa N, Yoshimura M. High-temperature x-ray study of the cubic-tetragonal diffusionless phase transition in the ZrO_2-$ErO_{1.5}$ system: I, phase change between two forms of a tetragonal phase, t′-ZrO_2 and t″-ZrO_2, in the compositionally homogeneous 14 mol% $ErO_{1.5}$-ZrO_2. *Journal of the American Ceramic Society*. 1993; 76(3): 641-648. Available from: https://doi.org/10.1111/j.1151-2916.1993.tb03654.x.

[10] Leger JM, Tomaszewski PE, Atouf A, Pereira AS. Pressure-induced structural phase transitions in zirconia under high pressure. *Physical Review B*. 1993; 47(21): 14075. Available from: https://doi.org/10.1103/PhysRevB.47.14075.

[11] Liu LG. New high pressure phases of ZrO_2 and HfO_2. *Journal of Physics and Chemistry of Solids*. 1980; 41(4): 331-334. Available from: https://doi.org/10.1016/0022-3697(80)90205-X.

[12] Yashima M, Mitsuhashi T, Takashina H, Kakihana M, Ikegami T, Yoshimura M. Tetragonal-monoclinic phase transition enthalpy and temperature of ZrO_2-CeO_2 solid solutions. *Journal of the American Ceramic Society.* 1995; 78(8): 2225-2228. Available from: https://doi.org/10.1111/j.1151-2916.1995.tb08642.x.

[13] Du Y, Jin Z, Huang P. Thermodynamic assessment of the ZrO_2-$YO_{1.5}$ system. *Journal of the American Ceramic Society*. 1991; 74(7): 1569-1577. Available from: https://doi.org/10.1111/j.1151-2916.1991.tb07142.x.

[14] Yashima M, Hirose T, Katano S, Suzuki Y, Kakihana M, Yoshimura M. Structural changes of ZrO_2-CeO_2 solid solutions around the monoclinic-tetragonal phase boundary. *Physical Review B*. 1991; 51(13): 8018. Available from: https://doi.org/10.1103/PhysRevB.51.8018.

[15] Clearfield A. Crystalline hydrous zirconia. *Inorganic Chemistry*. 1964; 3(1): 146-148. Available from: https://doi.org/10.1021/ic50011a034.

[16] Doroshkevich AS, Nabiev AA, Shylo AV, Pawlukojć A, Doroshkevich VS, Glazunova VA, et al. Frequency modulation of the Raman spectrum at the interface DNA-ZrO_2 nanoparticles. *Egyptian Journal of Chemistry*. 2019; 62: 13-20. Available from: https://doi.org/10.21608/EJCHEM.2019.12898.1806.

[17] Hladik J. *Physics of electrolytes* (Vol. 1). Academic Press Inc.,U.S., San Diego, CA, USA; 1972.

[18] Lughi V, Sergo V. Low temperature degradation-aging-of zirconia: A critical review of the relevant aspects in dentistry. *Dental Materials*. 2010; 26(8): 807-820. Available from: https://doi.org/10.1016/j.dental.2010.04.006.

[19] Kobayashi K, Kuwajima H, Masaki T. Phase change and mechanical properties of ZrO_2-Y_2O_3 solid electrolyte after ageing. *Solid State Ionics*. 1981; 3: 489-493. Available from: https://doi.org/10.1016/0167-2738(81)90138-7.

[20] Hohenberg P, Kohn W. Inhomogeneous electron gas. *Physical Review*. 1981; 136(3B): B864. Available from: https://doi.org/10.1103/PhysRev.136.B864.

[21] Perdew JP, Burke K, Ernzerhof M. Generalized gradient approximation made simple. *Physical Review Letters*.

1996; 77(18): 3865. Available from: https://doi.org/10.1103/PhysRevLett.77.3865.
[22] Sun J, Ruzsinszky A, Perdew JP. Strongly constrained and appropriately normed semilocal density functional. *Physical Review Letters*. 2015; 115(3): 036402. Available from: https://doi.org/10.1103/PhysRevLett.115.036402.
[23] Kresse G, Furthmüller J. Efficiency of ab-initio total energy calculations for metals and semiconductors using a plane-wave basis set. *Computational Materials Science*. 1996; 6(1): 15-50. Available from: https://doi.org/10.1016/0927-0256(96)00008-0.
[24] Howard CJ, Hill RJ, Reichert BE. Structures of ZrO_2 polymorphs at room temperature by high-resolution neutron powder diffraction. *Acta Crystallographica Section B: Structural Science*. 1988; 44(2): 116-120. Available from: https://doi.org/10.1107/S0108768187010279.
[25] Teufer G. The crystal structure of tetragonal ZrO_2. *Acta Crystallographica*. 1982; 15(11): 1187-1187. Available from: https://doi.org/10.1107/S0365110X62003114.
[26] Martin U, Boysen H, Frey F. Neutron powder investigation of tetragonal and cubic stabilized zirconia, TZP and CSZ, at temperatures up to 1400 K. *Acta Crystallographica Section B: Structural Science*. 1993; 49(3): 403-413. Available from: https://doi.org/10.1107/S0108768192011297.
[27] Martin U, Boysen H, Frey F. Neutron powder investigation of tetragonal and cubic stabilized zirconia, TZP and CSZ, at temperatures up to 1400 K. *Acta Crystallographica Section B: Structural Science*. 1993; 49(3): 403-413. Available from: https://doi.org/10.1107/S0108768192011297.
[28] Pascal R, Pross A. Stability and its manifestation in the chemical and biological worlds. *Chemical Communications*. 2015; 51(90): 16160-16165. Available from: https://doi.org/10.1039/C5CC06260H.
[29] Teter DM, Gibbs GV, Boisen Jr MB, Allan DC, Teter MP. First-principles study of several hypothetical silica framework structures. *Physical Review B*. 1995; 52(11): 8064. Available from: https://doi.org/10.1103/PhysRevB.52.8064.
[30] Heyd J, Scuseria GE, Ernzerhof M. Hybrid functionals based on a screened Coulomb potential. *The Journal of Chemical Physics*. 2003; 118(18): 8207-8215. Available from: https://doi.org/10.1063/1.1564060.
[31] Verma P, Truhlar DG. HLE16: A local Kohn-Sham gradient approximation with good performance for semiconductor band gaps and molecular excitation energies. *The Journal of Physical Chemistry Letters*. 2017; 8(2): 380-387. Available from: https://doi.org/10.1021/acs.jpclett.6b02757.
[32] Nematov DD, Kholmurodov KT, Husenzoda MA, Lyubchyk A, Burhonzoda AS. Molecular adsorption of H_2O on TiO_2 and TiO_2:Y surfaces. *Journal of Human, Earth, and Future*. 2022; 3(2): 213-222. Available from: http://dx.doi.org/10. 28991/HEF-2022-03-02-07.
[33] Nematov D. Influence of iodine doping on the structural and electronic properties of $CsSnBr_3$. *International Journal of Applied Physics*. 2022; 7: 36-47.
[34] Davlatshoevich ND. Investigation optical properties of the orthorhombic system $CsSnBr_{3-x}I_x$: Application for solar cells and optoelectronic devices. *Journal of Human, Earth, and Future*. 2021; 2(4): 404-411. Available from: https://doi.org/10.28991/HEF-2021-02-04-08.
[35] Davlatshoevich ND, Ashur KM, Saidali BA, KholmirzoTK, Lyubchyk A, Ibrahim M. Investigation of structural and optoelectronic properties of N-doped hexagonal phases of $TiO_2(TiO_{2-x}N_x)$ nanoparticles with DFT realization: Optimization of the band gap and optical properties for visible-light absorption and photovoltaic applications. *Biointerface Research in Applied Chemistry*. 2022; 12(3): 3836-3848. Available from: https://doi.org/10.33263/BRIAC123.38363848.
[36] Nematov DD, Burhonzoda AS, Khusenov MA, Kholmurodov KT, Yamamoto T. First principles analysis of crystal structure, electronic and optical properties of $CsSnI_{3-x}Br_x$ perovskite for photoelectric applications. *Journal of Surface Investigation: X-ray, Synchrotron and Neutron Techniques*. 2021; 15(3): 532-536. Available from: https://doi.org/10.1134/S1027451021030149.
[37] Davlatshoevich ND, Islomovich MB, Kholmirzo K. Optimization optoelectronic properties $Zn_xCd_{1-x}Te$ system for solar cell application: theoretical and experimental study. *Biointerface Research in Applied Chemistry*. 2022; 13(1). Available from: https://doi.org/10.33263/BRIAC131.090.
[38] Amondulloi B. DFT study on the electronic structure and optical properties of orthorhombic perovskite $CsPbBr_3$ doped with I and Cl. *Biointerface Research in Applied Chemistry*. 2023; 13(6): 516. Available from: https://doi.org/10.33263/BRIAC136.516.
[39] Nematov D, Burhonzoda A, Khusenov M, Kholmurodov K, Doroshkevych A, Doroshkevych N, et al. Molecular dynamics simulations of the DNA radiation damage and conformation behavior on a zirconium dioxide surface. *Egyptian Journal of Chemistry*. 2019; 62: 149-161. Available from: https://doi.org/10.21608/EJCHEM.2019.12981.1811.
[40] Nematov DD, Burhonzoda AS, Khusenov MA, Kholmurodov KT, Ibrahim MA. The quantum-chemistry

calculations of electronic structure of boron nitride nanocrystals with density functional theory realization. *Egyptian Journal of Chemistry*. 2019; 62: 21-27. Available from: https://ejchem.journals.ekb.eg/article_32161.html.

[41] Nematov DD, Burkhonzoda AS, Khusenov MA, Kholmurodov KT, Doroshkevich AS, Doroshkevich NV, et al. Molecular dynamics of DNA damage and conformational behavior on a zirconium-dioxide surface. *Journal of Surface Investigation: X-ray, Synchrotron and Neutron Techniques*. 2019; 13: 1165-1184. Available from: https://doi.org/10.1134/S1027451019060430.

[42] Nizomov Z, Asozoda M, Nematov D. Characteristics of nanoparticles in aqueous solutions of acetates and sulfates of single and doubly charged cations. *Arabian Journal for Science and Engineering*. 2023; 48(1): 867-873. Available from: https://doi.org/10.1007/s13369-022-07128-2.

[43] Danilenko I, Gorban O, Maksimchuk P, Viagin O, Malyukin Y, Gorban S, et al. Photocatalytic activity of ZnO nanopowders: The role of production techniques in the formation of structural defects. *Catalysis Today*. 2019; 328: 99-104. Available from: https://doi.org/10.1016/j.cattod.2019.01.021.

[44] Danilenko I, Gorban O, Viegas J, Shapovalova O, Akhkozov L, Lyubchyk S, et al. Photocatalytic composite nanomaterial and engineering solution for inactivation of airborne bacteria. *Topics in Catalysis*. 2021; 64: 772-779. Available from: https://doi.org/10.1007/s11244-020-01291-2.

[45] Dilshod N, Kholmirzo K, Aliona S, Kahramon F, Viktoriya G, Tamerlan K. On the optical properties of the $Cu_2ZnSn[S_{1-x}Se_x]_4$ system in the IR range. *Trends in Sciences*. 2023; 20(2): 4058-4058. Available from:https://doi.org/10.48048/tis.2023.4058.

[46] Petrov EG, Shevchenko YV, Snitsarev V, Gorbach VV, Ragulya AV, Lyubchik S. Features of superexchange nonresonant tunneling conductance in anchored molecular wires. *AIP Advances*. 2023; 9(11): 115120. Available from: https://doi.org/10.1063/1.5124386.

[47] Asgerov EB, Beskrovnyy AI, Doroshkevich NV, Mita C, Mardare DM, Chicea D, et al. Reversible martensitic phase transition in yttrium-stabilized ZrO_2 nanopowders by adsorption of water. *Nanomaterials*. 2022; 12(3): 435. Available from: https://doi.org/10.3390/nano12030435.